

## Catalysis

Layer by Layer Deposition of 1T'-MoS<sub>2</sub> for the Hydrogen Evolution ReactionFarbod Alimohammadi,<sup>[a, b]</sup> Parisa Yasini,<sup>[a, b]</sup> Tim Marshall,<sup>[a, b]</sup> Nuwan H. Attanayake,<sup>[a, b]</sup> Eric Borguet,<sup>[a, b]</sup> and Daniel R. Strongin\*<sup>[a, b]</sup>

The layer by layer (LbL) method has been used to assemble catalytic materials for the electrochemical hydrogen evolution reaction (HER). The electrocatalytic activity of LbL deposited 1T'-MoS<sub>2</sub> (metallic phase) on a fluorine-doped tin oxide substrate was investigated for the HER as a function of the number of deposition layers (mass loading). The morphology, thickness, and roughness of the deposited MoS<sub>2</sub> layers as a function of the number of deposition layers were investigated using atomic force microscopy and scanning electron microscopy. The average roughness of the surface increased with the number of deposition layers, indicating that the thickness of the deposited layered material became heterogeneous with increasing layer number. The primary conversion of the deposited 1T'-MoS<sub>2</sub> to the semiconducting 2H-MoS<sub>2</sub> phase via

exposure to 532 nm wavelength light, confirmed by Raman spectroscopy and scanning tunneling spectroscopy, allowed a comparison of the HER activity of the two phases at a constant mass loading and surface area on the same substrate. For a given number of deposition layers (i.e., similar mass loading), 1T'-MoS<sub>2</sub> exhibited a lower overpotential for the HER than the 2H-MoS<sub>2</sub> (with a minority 1T' component) phase. For example, at a sample thickness of 19.7 ± 2.8 nm (20 LbL layers) the overpotentials for the HER for submonolayer amounts of 1T'-MoS<sub>2</sub> and after exposure to 532 nm light were 0.54 and 0.61 V, respectively (at a current density of -2 mA/cm<sup>2</sup>). Overall, the overpotential for HER associated with both MoS<sub>2</sub> phases decreased as the mass loading increased.

## Introduction

Transition metal chalcogenides have attracted significant interest due to the earth-abundancy of the constituent elements and their favorable physical and chemical properties for potential use in technological applications.<sup>[1]</sup> Among this class of materials, molybdenum disulfide (MoS<sub>2</sub>) has been extensively studied due to its potential in energy storage, catalysis, and photodetectors.<sup>[2]</sup>

MoS<sub>2</sub> is a promising low-cost alternative to platinum-based catalysts for hydrogen production via the electrochemical hydrogen evolution reaction (HER), part of the water splitting process.<sup>[3]</sup> Two common 2D layered phases of MoS<sub>2</sub> are the 1T' (distorted metallic octahedral structure) and 2H (semiconducting trigonal prismatic structure),<sup>[4]</sup> and both phases have been studied for the HER.<sup>[5]</sup> In general, it has been shown that while

edge sites are active for electrocatalytic HER on both 2H and 1T' MoS<sub>2</sub> phases, basal planes are the primary HER-active sites on the metallic 1T'-phase.<sup>[6]</sup> The enhanced conductivity and likely the higher density of active catalytic sites contribute to the 1T'-phase exhibiting superior electrocatalytic kinetic parameters compared to the 2H-phase.<sup>[5a]</sup>

Perhaps, due to the structural stability of the 2H phase relative to the 1T' phase, there has been a greater effort in understanding the electrocatalytic activity of the 2H MoS<sub>2</sub> phase.<sup>[3b,6b, 7]</sup> Prior studies have investigated the layer dependence (controlled by using the chemical vapor deposition technique) of the 2H phase for the electrocatalytic HER<sup>[5c,8]</sup> and have shown that the single layer catalyst is more active compared to the few-layer catalyst. This observation was attributed to the relatively poor out of plane conductivity of the semiconducting phase which limits the electrocatalytic activity of layers spatially removed from the electrode surface.<sup>[8a]</sup>

In the present contribution, we investigated the HER activity of the conductive 1T' phase of MoS<sub>2</sub>. The MoS<sub>2</sub> was assembled by a layer-by-layer (LbL) deposition method using the sequential adsorption of negatively charged 1T'-MoS<sub>2</sub> 2D sheets and positively charged cations (Na<sup>+</sup>) that resided in the interlayer region between the 2D sheets. We note that similar LbL solution phase assembly methods have been used for various applications that include biomedical<sup>[9]</sup> and energy storage,<sup>[10]</sup> and water splitting.<sup>[11]</sup>

The goals of the research effort were two-fold. First, a goal was to determine the effect of mass loading, i.e. the number of deposition layers, on HER activity for the metallic 1T' phase of

[a] Dr. F. Alimohammadi, Dr. P. Yasini, T. Marshall, Dr. N. H. Attanayake, Prof. E. Borguet, Prof. D. R. Strongin  
Department of Chemistry  
Temple University  
Philadelphia, Pennsylvania  
19122, USA  
E-mail: daniel.strongin@temple.edu

[b] Dr. F. Alimohammadi, Dr. P. Yasini, T. Marshall, Dr. N. H. Attanayake, Prof. E. Borguet, Prof. D. R. Strongin  
Center for Complex Materials from First Principles (CCM)  
Temple University  
Philadelphia, Pennsylvania  
19122, USA

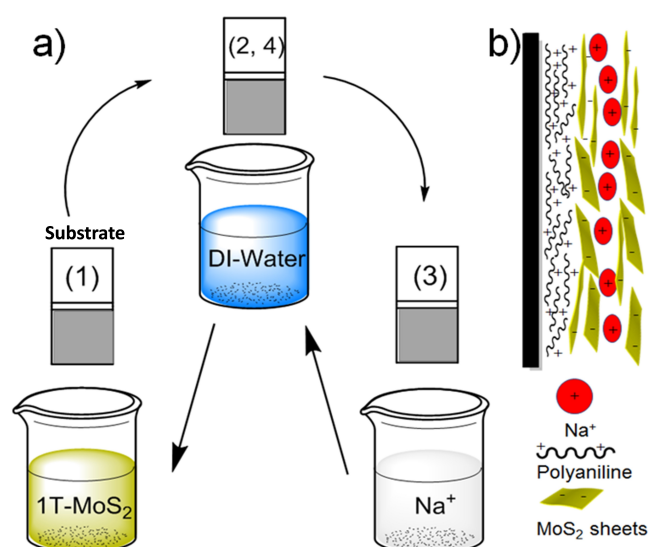
Supporting information for this article is available on the WWW under <https://doi.org/10.1002/slct.202103386>

MoS<sub>2</sub> (deposited on fluorine doped tin oxide (FTO) as shown in Scheme 1). The second goal was to directly compare the electrocatalytic HER activity of the metallic 1T' MoS<sub>2</sub> to the semiconducting 2H MoS<sub>2</sub> phase. A prior study showed that the exposure of 1T'-MoS<sub>2</sub> (few microns thick) to laser light from a commercial DVD optical drive could be used to transform the material to 2H-MoS<sub>2</sub>.<sup>[12]</sup> Along the same lines, our study used 532 nm laser light to convert few layer 1T'-MoS<sub>2</sub> to primarily 2H-MoS<sub>2</sub>. This strategy allowed us to directly compare the HER activity of the two pseudomorphic phases at a constant mass loading and surface area. Raman spectroscopy, atomic force microscopy (AFM), scanning electron microscopy (SEM), scanning tunneling microscopy (STM), and scanning tunneling spectroscopy (STS) were used to characterize the thickness, morphology, and electronic structure of the few-layer MoS<sub>2</sub> catalyst. Our results demonstrate that at equivalent mass loadings (and MoS<sub>2</sub> layer thicknesses), the 1T'-MoS<sub>2</sub> exhibited a lower overpotential for the HER than 2H-MoS<sub>2</sub>. Our study provides a novel approach to control the morphology and phase of MoS<sub>2</sub> sheets on the surface by the combination of LbL deposition and laser-induced transformation for the investigation of HER catalytic activity. Results from the study help to shed light on the effect of MoS<sub>2</sub> layer number and phase composition on the water splitting reaction.

## Results and Discussion

### AFM of LbL assembled MoS<sub>2</sub> layers

Analysis of AFM images recorded on an Au(111) coated mica substrate before (Figure 1a) and after the deposition of MoS<sub>2</sub> for 1, 2, 5, 10, and 20 LbL layers (Figure 1e–f) revealed an increasing height/thickness, surface roughness and coverage



**Scheme 1.** a) Schematic showing the deposition procedure to grow MoS<sub>2</sub> layers on polyaniline (PANI)/FTO. Individual films were prepared for study by using 1, 5, 10 or 20 deposition cycles (layer number), b) Schematic cross section of a two-layer assembled material on the FTO surface.

(Table 1) with increasing layer number. After one LbL deposition, the median height of the MoS<sub>2</sub> was  $1.9 \pm 0.6$  nm and after 20 LbL cycles, the median height increased to  $19.7 \pm 2.8$  nm. The results of a linear regression fit of the layer number vs. average height indicated that after each LbL cycle the thickness increased  $\sim 1$  nm. The AFM data shows that during each cycle both single and few layers materials were deposited on the surface. The analysis of the AFM images showed that the median height and the surface roughness increase, and the height distribution becomes wider after each deposition layer (Figure 1, Figure S5, and Table 1). While the average thickness of the deposited MoS<sub>2</sub> layers is relatively proportional to the layer number, it is important to keep in mind that the height distribution in each layer is significant. For example, after 20 layers the median height of the MoS<sub>2</sub> layers is  $\sim 20$  nm, but features as thin as 15 nm and as thick as 25 nm are present on the substrate (Figure S5 and Table 1). Also, AFM images (Figure 1, Figure S6 and Table 1) show that while the entire gold substrate is not covered by MoS<sub>2</sub> homogeneously, the surface area increases after every deposition layer, because of the addition of sheets to previously bare areas on the Au(111) substrate.

### SEM of LbL assembled MoS<sub>2</sub> layers

Using the LbL method we assembled MoS<sub>2</sub> layers on FTO and characterized the morphology of the films as a function of deposition layer with SEM. Deposition of the sheets was investigated on FTO since this substrate was more robust and conducive for use as an electrode support material to determine the electrochemical properties of the MoS<sub>2</sub> sheets. The intrinsic roughness of FTO, however, precluded meaningful height measurements by AFM. SEM micrographs of 1T'-MoS<sub>2</sub> sheets assembled on FTO and features due to layered MoS<sub>2</sub> are shown in Figure 2 after 5, 10, and 20 LbL layers. The associated energy dispersive spectroscopy data for the 20-layer MoS<sub>2</sub>/FTO sample shows the presence of Mo and S, confirming the presence of MoS<sub>2</sub> layers. The MoS<sub>2</sub> mass loading for each MoS<sub>2</sub>/FTO sample was determined by ICP-MS and data acquired from this technique showed that the MoS<sub>2</sub> loading on FTO increased linearly with the layer number (Figure S7), consistent with the rise of the height and coverage by AFM images. Both SEM and inductively coupled plasma mass spectrometry (ICP-MS) analy-

**Table 1.** Average roughness, median height and surface coverage of 1T'-MoS<sub>2</sub> assembled on the Au(111) coated Mica. Gwyddion software was used for the visualization and analysis of images. Error bars are the standard deviation of the roughness and height median determined from three different figures for each cycle.

Number of layers	Roughness average ( $R_s$ )	Height median (nm)	Coverage (%)
0	$0.4 \pm 0.1$	–	–
1	$1.0 \pm 0.4$	$1.9 \pm 0.6$	$2.1 \pm 0.3$
2	$0.9 \pm 0.3$	$3.1 \pm 0.7$	$7.7 \pm 0.9$
5	$1.5 \pm 1.0$	$4.6 \pm 1.0$	$9.2 \pm 2.1$
10	$2.0 \pm 1.0$	$10.5 \pm 1.4$	$25.6 \pm 3.2$
20	$3.9 \pm 2.3$	$19.7 \pm 2.8$	$38.7 \pm 10.3$

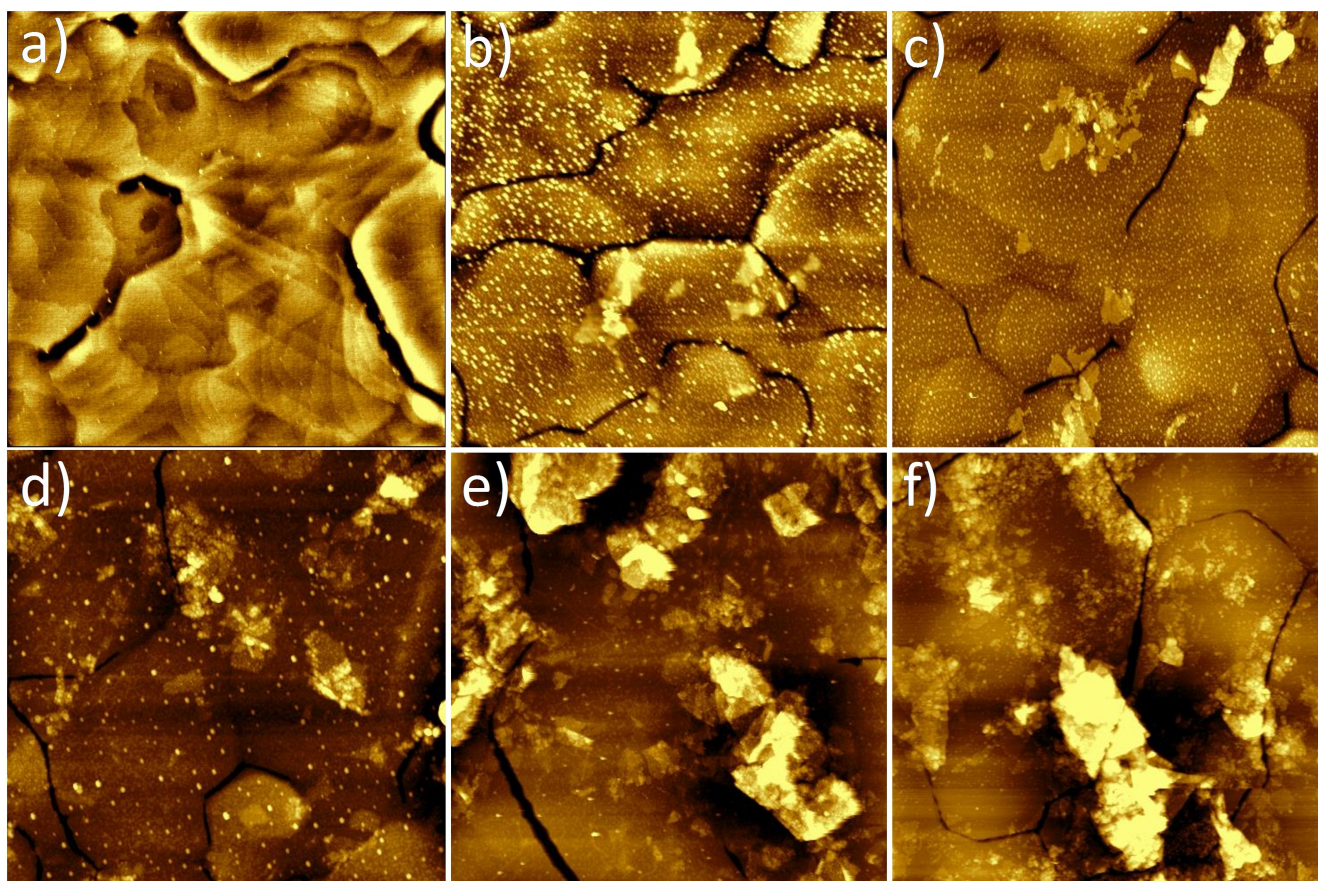


**Figure 1.** Topographic AFM images ( $2.5 \times 2.5 \mu\text{m}^2$ ) of the  $1\text{T}'\text{-MoS}_2$  layers assembled on the single crystal gold coated mica. a) bare Au substrate, b) one layer, c) two layers, d) five layers, e) ten layers, f) twenty layers.

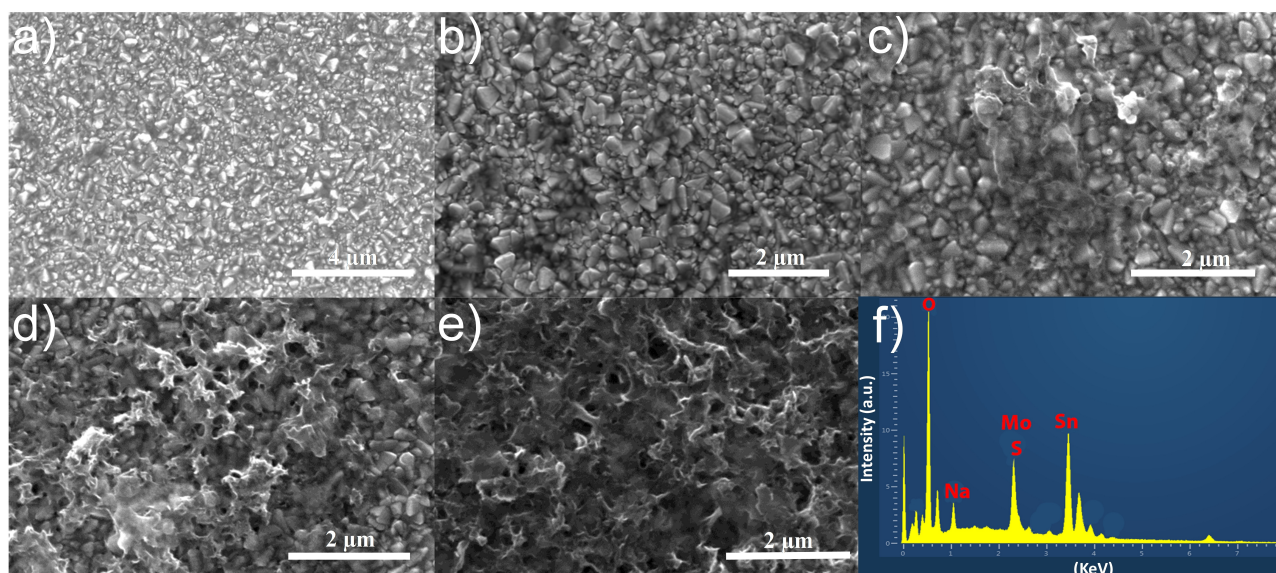


**Figure 2.** SEM images of a) bare FTO surface, b) 1 layer, c) 5 layers, d) 10 layers, e) 20 layers, assembled on the FTO surface f) EDAX spectra of 20 layers assembled  $1\text{T}'\text{-MoS}_2$ .

sis confirmed the formation of increasing numbers of layers with each deposition layer.

### Raman of LbL 1T'-MoS<sub>2</sub> and after conversion to 2H-MoS<sub>2</sub>

Previous studies have shown that Raman is a powerful technique to study monolayer and few layer MoS<sub>2</sub>.<sup>[13]</sup> The evolution of the assembled MoS<sub>2</sub> layers on the surface was studied ex-situ by Raman spectroscopy. The results for bulk 1T'-MoS<sub>2</sub> (Figure 3a), 1T'-MoS<sub>2</sub> layers on FTO (Figure 3b), and 2H-MoS<sub>2</sub> layers on FTO (Figure 3c) reveal the characteristic features of the different phases. Bulk 1T'-MoS<sub>2</sub> exhibits strong Raman peaks at 153, 220, 290, 328, 381, and 403 cm<sup>-1</sup> that are attributed to the J<sub>1</sub>, J<sub>2</sub>, E<sub>1g</sub>, J<sub>3</sub>, E<sub>2g</sub><sup>1</sup>, and A<sub>1g</sub> vibrational modes, respectively.<sup>[12,14]</sup> The E<sub>2g</sub><sup>1</sup> and A<sub>1g</sub> are characteristic peaks for 1T'-MoS<sub>2</sub> and 2H-MoS<sub>2</sub>, and are attributed to in-plane (intra-layer) and out-of-plane (interlayer) vibrations.<sup>[15]</sup> The J<sub>1</sub> mode at 153 cm<sup>-1</sup> is associated with the distorted octahedral structure of the 1T' phase of MoS<sub>2</sub>.<sup>[5c,14a,e]</sup> This particular mode is absent in the Raman spectrum of bulk 2H-MoS<sub>2</sub> (Figure S8).<sup>[5c,14e]</sup> The 2H phase has relatively strong E<sub>2g</sub><sup>1</sup> and A<sub>1g</sub> Raman modes at 380 and 406 cm<sup>-1</sup> (compared to the 1T' phase), respectively (Figure S8). Along with the J<sub>1</sub> mode, the J<sub>2</sub> and J<sub>3</sub> features are unique to the 1T' phase and are assigned to the superlattice structure in the basal plane of the monolayer MoS<sub>2</sub> that possess the distorted octahedral structure.<sup>[14d,15]</sup> The E<sub>1g</sub> and E<sub>2g</sub><sup>1</sup> vibrational modes are attributed to the octahedrally coordinated Mo in 1T'-MoS<sub>2</sub>.<sup>[3c]</sup> The Raman spectra of the MoS<sub>2</sub> verifies the presence of the 1T' phase.

Inspection of the Raman data for the one-layer LbL assembled MoS<sub>2</sub> in Figure 3b shows a weak A<sub>1g</sub> mode at 403 cm<sup>-1</sup>, but the 1T'-characteristic J<sub>1</sub>, J<sub>2</sub>, and J<sub>3</sub> modes are absent, presumably due to the low concentration of the deposited metal dichalcogenide. We attribute the broad mode(s) between 200 and 300 cm<sup>-1</sup> to the FTO substrate. After 5 LbL cycles, the A<sub>1g</sub> mode at 403 cm<sup>-1</sup> grows in intensity and the 1T'-characteristic J<sub>1</sub>, J<sub>2</sub>, and J<sub>3</sub> modes become apparent along with the E<sub>1g</sub> and E<sub>2g</sub><sup>1</sup> mode. Increasing the LbL cycles to 10 and then to 20 leads to a progressive increase in the

intensity of the Raman peaks associated with the 1T'-MoS<sub>2</sub> phase.

The phase transition of deposited MoS<sub>2</sub> layers from 1T' to 2H can be induced by exposure to laser light.<sup>[1,14b]</sup> This phase transformation is confirmed with Raman spectroscopy (Figure 3c). Perhaps, the most significant spectral change after the laser treatment is that the intensities of the E<sub>2g</sub><sup>1</sup> and A<sub>1g</sub> modes (Figure 3c) become greater than the respective Raman modes for the 1T' samples (Figure 3b). Furthermore, the J<sub>1</sub>, J<sub>2</sub>, and J<sub>3</sub> modes associated with 1T'-MoS<sub>2</sub> are absent after the phase conversion to 2H-MoS<sub>2</sub> (Figure 3c). All the spectra in Figure 3c are similar to the Raman spectra of the control 2H-MoS<sub>2</sub> sample (Figure S8). Although these data show that in each case the 1T' phase was primarily converted into 2H-MoS<sub>2</sub> during the 532 nm laser light irradiation, the careful examination of the 2H-MoS<sub>2</sub> after laser treatment using Raman spectroscopy indicates that there is a weak peak at J<sub>1</sub> position. The presence of the weak J<sub>1</sub> feature indicates that there is some 1T' MoS<sub>2</sub> within the primarily 2H-MoS<sub>2</sub> sample. SEM of MoS<sub>2</sub> deposited on FTO showed that the morphology of MoS<sub>2</sub> sheets did not change after converting the 1T' phase into the 2H phase (Figure S9).

### STM and STS of MoS<sub>2</sub> before and after conversion to 2H-MoS<sub>2</sub>

STS provides important information about the electronic structure of 2D-materials. For example, the general profile of the density of states around the Fermi level can be used to categorize materials based on their conductivities. To shed light on the local electronic properties of the 1T'-MoS<sub>2</sub>, 2H-MoS<sub>2</sub> sheets (after laser transition) and 2H-MoS<sub>2</sub> flakes (deposited by chemical vapor deposition (CVD)) we carried out STM and STS under ambient conditions (Figure 4). Comparison of the imaged flakes in Figure 4a and b show that the light exposure of 1T'-MoS<sub>2</sub> to form 2H-MoS<sub>2</sub> maintains the flake-like morphology of the MoS<sub>2</sub>. Metallic and semi-metallic materials do not show a gap between the occupied states (valence band) and unoccupied states (conduction band). 2H-MoS<sub>2</sub> is a semi-

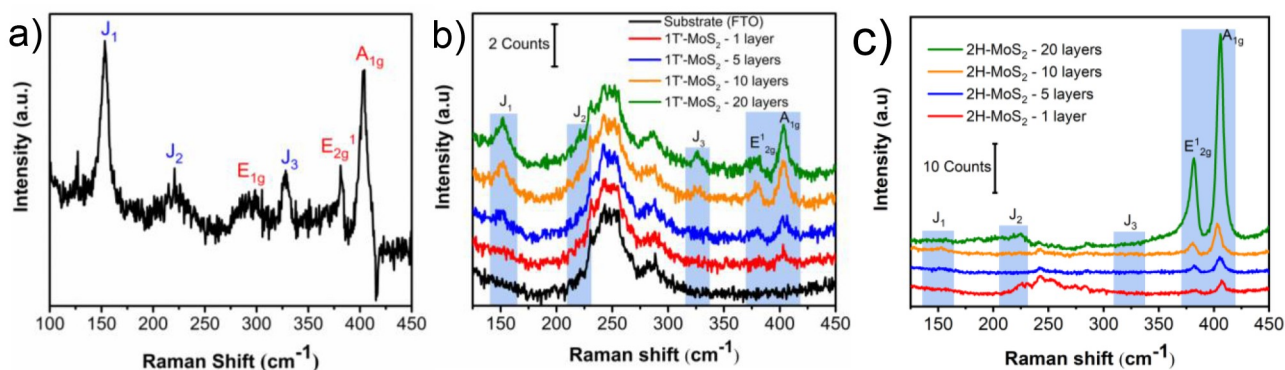


**Figure 3.** a) Raman spectra of bulk 1T'-MoS<sub>2</sub> on sapphire, b) Raman spectra of 1, 5, 10, and 20 layers 1T'-MoS<sub>2</sub> assembled on FTO, c) Raman spectra of 1, 5, 10, and 20 layer 2H-MoS<sub>2</sub> after laser-induced transformation.

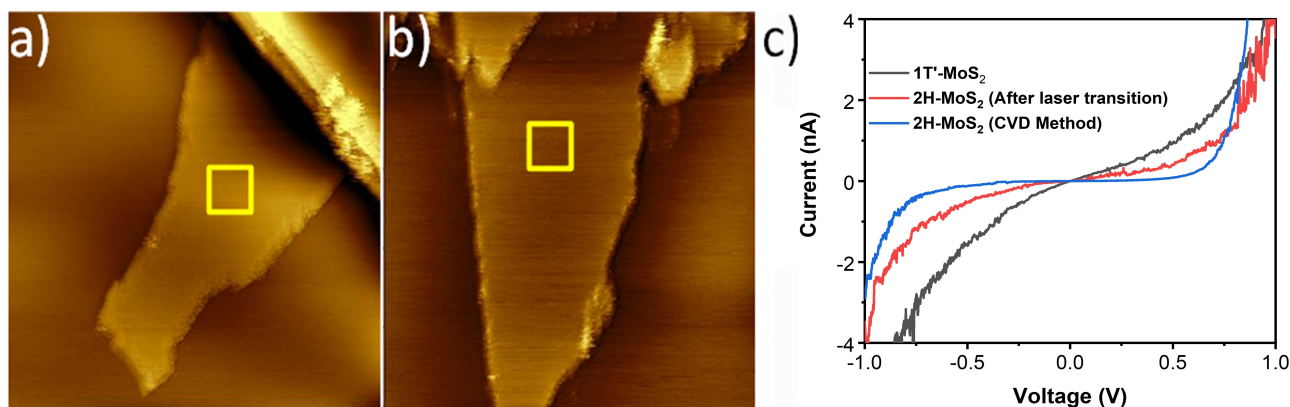


**Figure 4.** a) STM topography image of 1T'-MoS<sub>2</sub> on highly ordered pyrolytic graphite (HOPG) (0.10 × 0.10 μm<sup>2</sup>), b) 2H-MoS<sub>2</sub> formed after laser irradiation of 1T'-MoS<sub>2</sub> on HOPG, E<sub>bias</sub> = 300 mV, I<sub>t</sub> = 100 pA, (0.15 × 0.15 μm<sup>2</sup>), c) Average of 10 I–V response curves collected for the 1T'-MoS<sub>2</sub> and 2H-MoS<sub>2</sub> (after laser transition) and 2H-MoS<sub>2</sub> flakes (deposited by CVD method) on HOPG (yellow square indicates the area where the STS data was acquired).

conductor, and there is a gap between filled  $d_{z^2}$  and empty  $d_{x^2-y^2}$ ,  $d_{xy}$  orbitals of MoS<sub>2</sub>, while 1T'-MoS<sub>2</sub> does not show a gap between the occupied states (valance band) and unoccupied states (conduction band).<sup>[16]</sup> However, comparing the conductivity of the 2H-MoS<sub>2</sub> sheets (after laser transition) shows higher conductivity than 2H-MoS<sub>2</sub> flakes (deposited by CVD method). In this study, the tunneling current response vs. bias was recorded above the central area of the 1T'-MoS<sub>2</sub> sheets, spatially removed from any step edges and possible defects (Figure 4a and 4b). An average of ~ 10 I–V spectra were recorded on the MoS<sub>2</sub> sheets before and after the laser transformation process that converted the 1T' phase to the 2H phase. After laser irradiation (red solid line) which converts the 1T' phase to 2H-MoS<sub>2</sub>, an analysis of the STS data shows that there is the emergence of a band gap (~ 1 eV). The band gap of the 2H-MoS<sub>2</sub> flakes (deposited by the CVD method) is around 1.4 eV which is close to the values reported in the literature for the 2H phase (~ 1.6 eV).<sup>[17]</sup> The lower band gap measured for the laser transformed material most likely means that there is an incomplete transformation of the 1T'-MoS<sub>2</sub> into the 2H phase during laser irradiation, consistent with Raman data discussed before. This result indicates that the MoS<sub>2</sub> band gap could be tuned by laser exposure and is sensitive to physical and chemical modifications. To the best of our knowledge, the experimental measurement of the tunneling conductance of

1T'-MoS<sub>2</sub> in an ambient environment is reported here for the first time (Figure 4c).

#### Electrocatalytic activity of MoS<sub>2</sub> layers for the HER

The HER activity of the assembled 1T'-MoS<sub>2</sub> and 2H-MoS<sub>2</sub> (formed via the laser irradiation of the 1T' phase) on FTO was experimentally investigated by recording polarization curves (Figure 5). Perhaps the most significant conclusions that can be drawn from an inspection of the polarization data are 1) at a particular MoS<sub>2</sub> film thickness, the 1T' phase shows a lower overpotential than the 2H phase, and 2) for a given MoS<sub>2</sub> phase the overpotential decreases with the number of deposition layers. At a MoS<sub>2</sub> thickness of ~ 1 nm, the 1T' phase exhibited an HER overpotential of 0.67 V (at a cathodic current of  $-2 \text{ mA cm}^{-2}$ ) compared to 0.71 V for the same thickness 2H-MoS<sub>2</sub> sample (Table 2). It is important to mention that typical overpotentials for bulk 1T'-MoS<sub>2</sub> and 2H-MoS<sub>2</sub> are closer to 200 mV and 400 mV, respectively, at  $-10 \text{ mA cm}^{-2}$ .<sup>[5b,18]</sup> For example, 1T' flakes that were restacked into bulk material by drying and deposited onto a glassy carbon electrode exhibited an overpotential of 230 mV<sup>14c</sup>. We attribute the reduced cathodic current and higher overpotentials reported here being due to the submonolayer (40% of the surface is covered after 20 MoS<sub>2</sub> layers) amounts of 1T'-MoS<sub>2</sub> flakes used in our study with a correspondingly smaller mass than what was used in

**Table 2.** Summary of electrochemical data of 1T'-MoS<sub>2</sub> before and after conversion to 2H-MoS<sub>2</sub> and average MoS<sub>2</sub> mass on the FTO electrode surface.

Samples	Overpotential (V) at $2 \text{ mA cm}^{-2}$	Overpotential (V) at $2 \text{ mA cm}^{-2}$ after laser treatment	Onset potential (V)	Onset potential (V) after laser treatment	Charge transfer resistance ( $\Omega$ )	C <sub>dl</sub> ( $\text{mF cm}^{-2}$ )	Average MoS <sub>2</sub> mass ( $\mu\text{g cm}^{-2}$ )
1 layer	0.67	0.71	0.50	0.57	712.3	0.051	0.15
5 layers	0.63	0.72	0.48	0.56	543.1	0.053	0.33
10 layers	0.59	0.66	0.44	0.53	169.4	0.112	0.51
20 layers	0.54	0.61	0.42	0.49	69.9	0.177	0.86

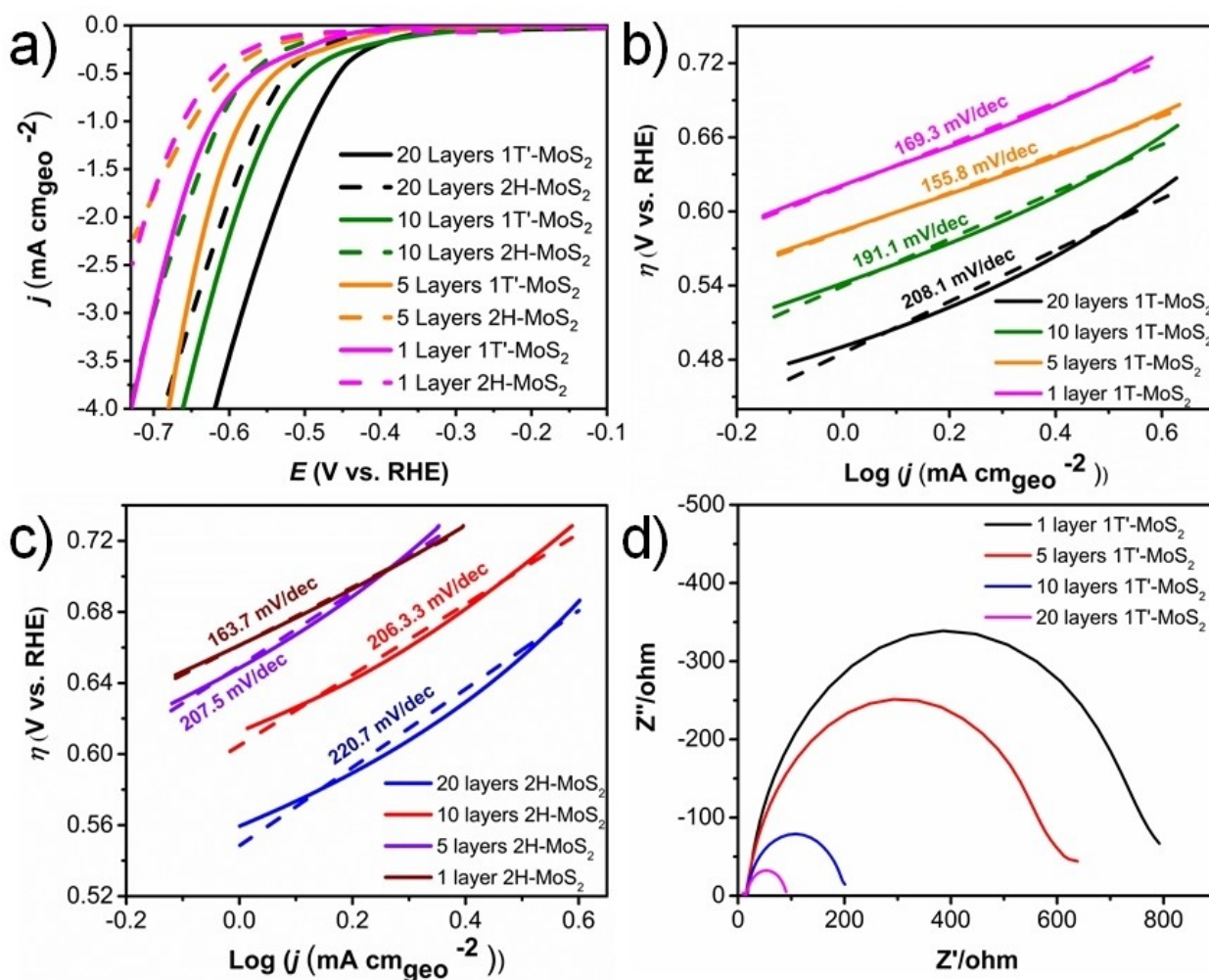


**Figure 5.** a) Polarization curves of 1T' and 2H-MoS<sub>2</sub> layers assembled on FTO for HER (The potential sweep rate was 10 mV·s<sup>-1</sup>), Tafel plots for b) 1T'-MoS<sub>2</sub>, and c) 2H-MoS<sub>2</sub>, and d) Nyquist plots of the 1T'-MoS<sub>2</sub> assembled layers.

prior studies. The effect of mass loading on the HER kinetics is discussed below. It is also mentioned that PANI was used to bind the layers to the Au surface which might also introduce increased electrical resistance.

The difference in the HER overpotentials for the two phases of MoS<sub>2</sub> was maintained up to the highest layer number samples (Table 2). This result that 1T'-MoS<sub>2</sub> exhibits a lower HER overpotential than the 2H phase is in general agreement with prior studies.<sup>[5a,b, 6b]</sup> However, we point out that in contrast to prior comparisons of these two phases for HER, the present study compares the HER activity of the 1T' and 2H phases at identical loadings and layer numbers. Supported by the STS results (Figure 4), we propose that the higher HER overpotential associated with 2H-MoS<sub>2</sub> is likely due to its higher electrical resistance, compared to the semi-metallic electrical properties of the 1T' which could lead to an enhanced electron transport processes within and between layers critical for electrocatalysis. We did not observe the large overpotential difference of the 1T'-MoS<sub>2</sub> and 2H-MoS<sub>2</sub> which we believe is due to the incomplete transition of the 1T' phase to 2H after laser-induced

transformation. Prior studies have suggested that the metallic 1T' phase can utilize both basal and edge sites to catalyze HER<sup>[5a,18a]</sup> and this experimental observation is likely due in part to the metallic-like electrical conductivity of the 1T' phase.

In contrast to the overpotential trend, the Tafel slopes for both the 1T' and 2H-MoS<sub>2</sub> layered systems increase with the deposition layer number (Figure 5 b, c). Tafel slopes of 1T'-MoS<sub>2</sub> increase from 170 mV/dec for low LbL cycle number to 208 mV/dec at the highest deposition layer number. A similar relationship between decreasing overpotential and increasing Tafel slope with catalyst mass has been highlighted in prior studies of amorphous MoS<sub>2</sub> catalyst.<sup>[19]</sup> The relatively poor electron and mass transport properties of larger MoS<sub>2</sub> particles or thicker MoS<sub>2</sub> films manifest itself in an increasing Tafel slope with catalyst loading.<sup>[19–20]</sup> The decreasing overpotential with increasing MoS<sub>2</sub> loading, results from the increasing roughness (Table 1) and exchange current associated with higher mass loading.<sup>[19–20]</sup> In short, due to the increasing exchange current with mass loading, higher current densities are associated with the higher layer number samples at a given electrode potential

relative to smaller mass loading samples at that same potential. An analysis of the double layer capacitance ( $C_{dl}$ ) of the electrodes, associated with the formation of the electric double layer at the electrode/electrolyte interface<sup>[21]</sup> (Table 2) supports this contention. The rise in double layer capacitance with mass loading is associated with an increase in the redox-active surface due to the increase of height and the fraction of the surface covered by a single layer or multilayer MoS<sub>2</sub> sheets, as demonstrated by the analysis of AFM images (Figure 1 and Table 1). As pointed out in the prior studies the scalability of such a catalytic system is complicated since the increase in mass loading leads to a lower overpotential, but also to an increased Tafel slope, indicative of a suppressed electron and/or mass transport.<sup>[19–20]</sup>

To determine the charge transfer resistance of the electrode after each deposition layer, impedance spectroscopy was applied to distinguish charge transfer resistance ( $R_{ct}$ ) from other resistances.<sup>[22]</sup> As shown in Figure 5d and Table 2,  $R_{ct}$  decreased from 712  $\Omega$  (1 layer) to 70  $\Omega$  (20 layers), with increasing MoS<sub>2</sub> deposition layers (or loading), consistent with the polarization curve results showing that HER performance improves with an increase in the number of deposition layers. As pointed out in prior research,  $R_{ct}$  is inversely proportional to current and hence is dependent on the surface area and/or loading of the electrocatalyst on the electrode.<sup>[23]</sup> The results show that  $C_{dl}$ , which is proportional to the catalyst surface area, increases with loading consistent with the decreasing  $R_{ct}$  (Table 1).

Polarization curves for the four different layered 1T'-MoS<sub>2</sub> electrocatalysts that were normalized to mass (Figure S10), show a similar trend for the overpotential and Tafel slope with layer number as the data normalized to the geometric surface area of the electrode (Figure 5a). While we are not certain of the underlying reason, this result does suggest that the 20-layer catalyst is intrinsically more active than a single layer, for example. Presumably, this is at least in part due to the creation of the 3D morphology that may introduce unique sites for HER that are not present on a single sheet. Certainly, the creation of interlayer space occurs, and this may be advantageous for the HER. Prior studies, for example, have shown that the HER on layered 1T'-MoS<sub>2</sub> is facilitated through the placement of alkali metal cations or 3d transition metal in the interlayer region.<sup>[8a,18b]</sup> Our MoS<sub>2</sub> layer materials contain alkali metal cations (Na<sup>+</sup>) in the interlayer region and it is possible that this facilitates the HER as the layer number increases. It is perhaps useful to bring forward a prior study that investigated the HER activity of well-defined chemical vapor deposited monolayer, bilayer, and trilayer pure 2H-MoS<sub>2</sub>.<sup>[8a]</sup> It was shown that the HER activity was strongly suppressed by increasing the layer number and this was rationalized by arguing that the out of plane conductivity of layered MoS<sub>2</sub> is limited and that layers more distant from the electrode surface are less able to kinetically compete in the redox charge transfer processes critical for the electrochemical reaction (HER).<sup>[8a]</sup> We suspect that the comparative roughness of our samples and the alkali metal cation intercalants are responsible for the increasing HER activity with layer number that is experimentally observed for our MoS<sub>2</sub> electrocatalytic system.

## Conclusions

The LbL method has been used to assemble catalytic materials for the electrochemical HER for the first time. 1T'-MoS<sub>2</sub> layers were successfully assembled on various substrates by the LbL technique. AFM analysis of the assembled films showed that the median height of the MoS<sub>2</sub> layers increased and the height distribution became broader after each deposition layer. The overpotentials associated with the electrocatalytic activity for the HER of 1T'-MoS<sub>2</sub>, as well as 2H-MoS<sub>2</sub> formed via the laser-induced conversion of 1T'-MoS<sub>2</sub>, were determined as a function of the number of deposition layers. The onset potential and the overpotential for HER decreased with an increase of the number of LbL deposition cycles for both phases. The 1T' phase of MoS<sub>2</sub> exhibited a lower HER overpotential than the 2H phase for a given deposition layer number (i.e., at equivalent mass loading). The electronic properties of MoS<sub>2</sub> monolayer sheets were determined by STS, and the results indicated that the 1T'-MoS<sub>2</sub> sheet was semi-metallic and the 2H-MoS<sub>2</sub> has semiconductor properties. Our study provides a new way to understand the formation of MoS<sub>2</sub> layers on the surface, the impact of surface area, and their HER-performance for water splitting electrocatalysis and future renewable energy technologies.

## Supporting Information Summary

The experimental section and additional material and surface characterization are available in supplementary information.

## Acknowledgements

*This work was supported by the Center for the Computational Design of Functional Layered Materials, an Energy Frontier Research Center funded by the U.S. Department of Energy, Office of Science, and Basic Energy Sciences under Award No. DESC0012575. We are grateful to Ali Behbahani for performing inductively coupled plasma-mass spectrometry. We acknowledge the use of services and facilities of Temple Materials Institute at Temple University.*

## Conflict of Interest

The authors declare no conflict of interest.

**Keywords:** 1T'-MoS<sub>2</sub> · hydrogen evolution reaction · layer-by-layer · scanning probe microscope · surface analysis

- [1] M. Chhowalla, H. S. Shin, G. Eda, L. J. Li, K. P. Loh, H. Zhang, *Nat. Chem.* **2013**, *5*, 263–275.  
[2] a) X. Li, H. W. Zhu, *J. Mater.* **2015**, *1*, 33–44; b) Z. Wang, B. Mi, *Environ. Sci. Technol.* **2017**, *51*, 8229–8244; c) W. Zhang, C. P. Chuu, J. K. Huang, C. H. Chen, M. L. Tsai, Y. H. Chang, C. T. Liang, Y. Z. Chen, Y. L. Chueh, J. H. He, M. Y. Chou, L. J. Li, *Sci. Rep.* **2014**, *4*, 1–8; d) S. Shit, S. Chhetri, S. Bolar, N. C. Murmu, W. Jang, H. Koo, T. Kaila, *ChemElectroChem* **2019**, *6*, 430–438; e) Y. Wang, W. Sun, X. Ling, X. Shi, L. Li, Y. Deng, C. An, X. Han, *Chemistry* **2019**, *25*, 1–8.

- [3] a) J. Kibsgaard, Z. Chen, B. N. Reinecke, T. F. Jaramillo, *Nat. Mater.* **2012**, *11*, 963–969; b) M. Zeng, Y. G. Li, *J. Mater. Chem. A* **2015**, *3*, 14942–14962; c) Q. Ding, B. Song, P. Xu, S. Jin, *Chem* **2016**, *1*, 699–726; d) S. Bolar, S. Shit, N. C. Murmu, T. Kuila, *ChemElectroChem* **2020**, *7*, 336–346.
- [4] a) E. Benavente, M. A. Santa Ana, F. Mendiza'bal, G. Gonzalez, *Coord. Chem. Rev.* **2002**, *224*, 87–109; b) H. H. Huang, X. Fan, D. J. Singh, W. T. Zheng, *Phys. Chem. Chem. Phys.* **2018**, *20*, 26986–26994.
- [5] a) M. A. Lukowski, A. S. Daniel, F. Meng, A. Forticaux, L. Li, S. Jin, *J. Am. Chem. Soc.* **2013**, *135*, 10274–10277; b) D. Voiry, M. Salehi, R. Silva, T. Fujita, M. W. Chen, T. Asefa, V. B. Shenoy, G. Eda, M. Chhowalla, *Nano Lett.* **2013**, *13*, 6222–6227; c) J. Zhang, J. Wu, H. Guo, W. Chen, J. Yuan, U. Martinez, G. Gupta, A. Mohite, P. M. Ajayan, J. Lou, *Adv. Mater.* **2017**, *29*, 1–7.
- [6] a) G. Q. Li, D. Zhang, Q. Qiao, Y. F. Yu, D. Peterson, A. Zafar, R. Kumar, S. Curtarolo, F. Hunte, S. Shannon, Y. M. Zhu, W. T. Yang, L. Y. Cao, *J. Am. Chem. Soc.* **2016**, *138*, 16632–16638; b) T. F. Jaramillo, K. P. Jorgensen, J. Bonde, J. H. Nielsen, S. Horch, I. Chorkendorff, *Science* **2007**, *317*, 100–102.
- [7] C. Liu, X.-Y. Cui, Y.-H. Song, M.-L. Zhu, Z.-T. Liu, Z.-W. Liu, *ChemCatChem* **2019**, *11*, 1112–1122.
- [8] a) Y. Yu, S. Y. Huang, Y. Li, S. N. Steinmann, W. Yang, L. Cao, *Nano Lett.* **2014**, *14*, 553–558; b) E. Parzinger, E. Mitterreiter, M. Stelzer, F. Kreupl, J. W. Ager, A. W. Holleitner, U. Wurstbauer, *Appl. Mater. Res.* **2017**, *8*, 132–140.
- [9] a) J. J. Richardson, J. Cui, M. Bjornmalm, J. A. Braunger, H. Ejima, F. Caruso, *Chem. Rev.* **2016**, *116*, 14828–14867; b) J. J. Richardson, M. Bjornmalm, F. Caruso, *Science* **2015**, *348*, 1–11; c) H. Ai, S. A. Jones, Y. M. Lvov, *Cell Biochem. Biophys.* **2003**, *39*, 23–43.
- [10] a) T. Lee, S. H. Min, M. Gu, Y. K. Jung, W. Lee, J. U. Lee, D. G. Seong, B. S. Kim, *Chem. Mater.* **2015**, *27*, 3785–3796; b) E. Ahn, T. Lee, M. Gu, M. Park, S. H. Min, B.-S. Kim, *Chem. Mater.* **2016**, *29*, 69–79; c) Y. Xiang, S. Lu, S. P. Jiang, *Chem. Soc. Rev.* **2012**, *41*, 7291–7321.
- [11] G. E. Fenoya, E. Mazaa, E. Zelayad, W. A. Marmisolléa, O. Azzaroni, *Appl. Surf. Sci.* **2017**, *416*, 24–32.
- [12] X. B. Fan, P. T. Xu, D. K. Zhou, Y. F. Sun, Y. G. C. Li, M. A. T. Nguyen, M. Terrones, T. E. Mallouk, *Nano Lett.* **2015**, *15*, 5956–5960.
- [13] a) H. Li, Q. Zhang, C. C. R. Yap, B. K. Tay, T. H. T. Edwin, A. Olivier, D. Baillargeat, *Adv. Funct. Mater.* **2012**, *22*, 1385–1390; b) S. Mignuzzi, A. J. Pollard, N. Bonini, B. Brennan, I. S. Gilmore, M. A. Pimenta, D. Richards, D. Roy, *Phys. Rev. B* **2015**, *91*, 1–6.
- [14] a) N. Papadopoulos, G. A. Steele, H. S. J. van der Zant, *Phys. Rev. B* **2017**, *96*, 1–5; b) G. Eda, H. Yamaguchi, D. Voiry, T. Fujita, M. Chen, M. Chhowalla, *Nano Lett.* **2011**, *11*, 5111–5116; c) N. H. Attanayake, A. C. Thenuwara, A. Patra, Y. V. Aulin, T. M. Tran, H. Chakraborty, E. Borguet, M. L. Klein, J. P. Perdew, D. R. Strongin, *ACS Energy Lett.* **2018**, *3*, 7–13; d) S. J. Sandoval, D. Yang, R. F. Frindt, J. C. Irwin, *Phys. Rev. B* **1991**, *44*, 3955–3962; e) M. Calandra, *Phys. Rev. B* **2013**, *88*, 1–6.
- [15] a) D. Voiry, A. Mohite, M. Chhowalla, *Chem. Soc. Rev.* **2015**, *44*, 2702–2712; b) D. Yang, S. J. Sandoval, W. M. Divigalpitiya, J. C. Irwin, R. F. Frindt, *Phys. Rev. B* **1991**, *43*, 12053–12056.
- [16] Z. K. Tang, H. Zhang, H. Liu, W. M. Lau, L. M. Liu, *J. Appl. Phys.* **2014**, *115*, 204302.
- [17] a) A. Bruix, J. A. Miwa, N. Hauptmann, D. Wegner, S. Ulstrup, S. S. Grønberg, C. E. Sanders, M. Dendzik, A. Grubišić Čabo, M. Bianchi, J. V. Lauritsen, A. A. Khajetoorians, B. Hammer, P. Hofmann, *Phys. Rev. B* **2016**, *93*, 1–10; b) B. Ouyang, Z. Mi, J. Song, *J. Phys. Chem. C* **2016**, *120*, 8927–8935.
- [18] a) J. D. Benck, T. R. Hellstern, J. Kibsgaard, P. Chakthranont, T. F. Jaramillo, *ACS Catal.* **2014**, *4*, 3957–3971; b) N. H. Attanayake, A. C. Thenuwara, A. Patra, Y. V. Aulin, T. M. Tran, H. Chakraborty, E. Borguet, M. L. Klein, J. P. Perdew, D. R. Strongin, *ACS Energy Lett.* **2017**, *3*, 7–13.
- [19] a) H. Vrabel, T. Moehl, M. Gratzel, X. Hu, *Chem. Commun.* **2013**, *49*, 8985–8987; b) A. P. Murthy, J. Theerthagiri, J. Madhavan, K. Murugan, *Phys. Chem. Chem. Phys.* **2017**, *19*, 1988–1998; c) Z. W. Seh, J. Kibsgaard, C. F. Dickens, I. Chorkendorff, J. K. Nørskov, T. F. Jaramillo, *Science* **2017**, *355*, 1–12.
- [20] J. D. Benck, Z. Chen, L. Y. Kuritzky, A. J. Forman, T. F. Jaramillo, *ACS Catal.* **2012**, *2*, 1916–1923.
- [21] B. A. Mei, O. Munteshari, J. Lau, B. Dunn, L. Pilon, *J. Phys. Chem. C* **2018**, *122*, 194–206.
- [22] I. I. Suni, *TrAC Trends Anal. Chem.* **2008**, *27*, 604–611.
- [23] S. P. Zankowski, P. M. Vereecken, *J. Electrochem. Soc.* **2019**, *166*, D227–D235.

Submitted: September 22, 2021

Accepted: January 27, 2022